Title

Characterization of Uranyl Coordinated by Equatorial Oxygen: Oxo in UO3 versus Oxyl in UO3 +

Permalink

https://escholarship.org/uc/item/8jk5w3j7

Journal

The Journal of Physical Chemistry A, 125(25)

ISSN

1089-5639

Authors

Renault, Eric
Jian, Jiwen
Maurice, Rémi
et al.

Publication Date

2021-07-01

DOI

10.1021/acs.jpca.1c03818

Peer reviewed

Characterization of Uranyl Coordinated by Equatorial Oxygen: Oxo in UO_3 versus Oxyl in UO_3^+

Eric Renault,[1,*] Jiwen Jian,[2] Rémi Maurice,[3] Michael J. van Stipdonk,[4,*] Irena J. Tatosian,[4] Amanda R. Bubas,[4] Jonathan Martens,[5] Giel Berden,[5] Jos Oomens,[5,6] and John K. Gibson[2,*]

[1] CEISAM UMR 6230, CNRS, Université de Nantes, F-44000 Nantes, France

[2] Chemical Sciences Division, Lawrence Berkeley National Laboratory, Berkeley, California 94720, United States

[3] SUBATECH, UMR CNRS 6457, IN2P3/IMT Atlantique/Université de Nantes, 4 rue Alfred Kastler, BP 20722, 44307 Nantes Cedex 3, France

[4] Department of Chemistry and Biochemistry, Duquesne University, 600 Forbes Ave, Pittsburgh PA 15282 United States

[5] Radboud University Nijmegen, Institute for Molecules and Materials, FELIX Laboratory, Toernooiveld 7, 6525ED Nijmegen, The Netherlands

[6] van 't Hoff Institute for Molecular Sciences, University of Amsterdam, Science Park 904, 1098XH Amsterdam, The Netherlands

*Corresponding author email:
Eric.Renault@univ-nantes.fr; vanstipdonkm@duq.edu; jkgibson@lbl.gov

Abstract

Uranium trioxide, UO_3, has a T-shaped structure with bent uranyl, UO_2^{2+}, coordinated by an equatorial oxo, O^{2-}. The structure of cation UO_3^+ is similar but with an equatorial oxyl, $O^{\bullet -}$. Neutral and cationic uranium trioxide coordinated by nitrates were characterized by collision induced dissociation (CID), infrared multiple-photon dissociation (IRMPD) spectroscopy, and density functional theory. CID of uranyl nitrate, $\mathbf{[UO_2(NO_3)_3]^-}$ (complex ***A1***), eliminates NO_2 to produce nitrate-coordinated UO_3^+, $\mathbf{[UO_2(O^\bullet)(NO_3)_2]^-}$ (***B1***), which ejects NO_3 to yield UO_3 in $\mathbf{[UO_2(O)(NO_3)]^-}$ (***C1***). Finally, ***C1*** associates with H_2O to afford uranyl hydroxide in $\mathbf{[UO_2(OH)_2(NO_3)]^-}$ (***D1***). IRMPD of ***B1***, ***C1*** and ***D1*** confirms uranyl equatorially coordinated by nitrate(s) along with the following ligands: (***B1***) radical oxyl $O^{\bullet -}$; (***C1***) oxo O^{2-}; and (***D1***) two hydroxyls, OH^-. As the nitrates are bidentate, the equatorial coordination is six in ***A1***, five in ***B1***, four in ***D1*** and three in ***C1***. Ligand congestion in low-coordinate ***C1*** suggests orbital-directed bonding. Hydrolysis of the equatorial oxo in ***C1*** epitomizes the inverse trans influence in UO_3, which is uranyl with inert axial oxos and a reactive equatorial oxo. The uranyl ν_3 IR frequencies indicate the following donor ordering: O^{2-} *[best donor]* $>>$ $O^{\bullet -} > OH^- > NO_3^-$.

Introduction

Uranium chemistry is dominated by the hexavalent oxidation state afforded by the linear uranyl dication, which possesses highly stable axial oxo bonds, $[O_{yl}=U=O_{yl}]^{2+}$, that are progressively weakened by increased equatorial coordination.[1, 2] Lower $U=O_{yl}$ bond strength is indicated by longer bond length, red-shifting of the characteristic uranyl ν_2 and ν_3 stretch frequencies, and enhanced reactivity.[3-11] A particularly elementary uranyl coordination scenario is a single equatorial oxo-ligand, O^{2-}, which yields neutral UO_3 that can alternatively be designated as "uranyl oxide".[1] Uranium trioxide is a vapor species under high temperature conditions, making the gas-phase reactivity of UO_3 particularly relevant to nuclear material processing and mishaps.[12, 13] The T-shaped structure of UO_3 has been confirmed by IR spectroscopy in inert matrices, validating the description as bent UO_2^{2+} coordinated by equatorial O^{2-}.[14-18] The C_{2v} structure of UO_3 contrasts with typical D_{3h} transition metal trioxides with three equivalent oxo groups.[19, 20] All three oxo groups in UO_3 have large bond dissociation energies (*BDEs*):[21, 22] *BDE*[U-O] = 758 kJ/mol; *BDE*[OU-O] = 750 kJ/mol; and *BDE*[O_2U-O] = 603 kJ/mol. The first two correspond to very strong axial $U=O_{yl}$, while the third is associated with the weaker equatorial $U=O_{eq}$, a relationship that makes UO_3 a prototypical case of the actinide inverse-trans effect.[23] The *BDEs* for oxide cation XO^+ and neutral XO are related by ionization energies (IEs): *BDE*[X^+-O] = *BDE*[X-O] – (IE[XO] – IE[X]). This relationship provides the following *BDEs* for uranium oxide cations:[22, 24] *BDE*[U^+-O] = 774 kJ/mol; *BDE*[OU^+-O] = 741 kJ/mol; *BDE*[O_2U^+-O] = 172 kJ/mol. The similarity between the *BDEs* for neutral and cationic $UO^{0/+}$ and $UO_2^{0/+}$ reflects that ionization removes a non-bonding electron. In contrast, hexavalent uranium in UO_3 is in its highest oxidation state, such that a bonding electron is ionized, with as a consequence that the *BDE* for the disrupted bond in UO_3^+ is greatly reduced, from 603 kJ/mol for UO_3 to 172 kJ/mol for UO_3^+. The structure of UO_3^+ has not been determined, but is predicted to be T-shaped like neutral UO_3, though with an equatorial oxyl, $U\text{-}O^{\bullet}_{eq}$.[25] Such a switch from $U=O_{eq}$ in UO_3 to $U\text{-}O^{\bullet}_{eq}$ in UO_3^+ is consistent with the corresponding drastic decrease in *BDE*. Although these structures and bonding concepts for UO_3 and UO_3^+ are in accord with known thermodynamics, there is no direct characterization of the postulated oxyl in UO_3^+.

Solid uranium trioxide, UO_3*(s)*, exhibits six allotropes and is important in nuclear fuel cycles.[26-28] Although the allotropes are not simple assemblies of molecular UO_3, the structures do exhibit characteristics of uranyl moieties equatorially coordinated by oxygen.[29, 30] Hydration of solid UO_3 under ambient conditions ultimately forms minerals such as shoepite.[31, 32] A key consideration for UO_3*(s)* behavior is kinetics for transformation of its hydrate $UO_3(H_2O)$ to hydroxide $UO_2(OH)_2$.[33-39] Hydroxides such as found in minerals are thermodynamically more stable than hydrates of uranium trioxide,[38] but mechanisms of the hydrate-to-hydroxide transformations on timescales shorter than geological and thus more relevant to material storage and processing are poorly understood.[39]

Although uranyl coordination chemistry is studied primarily in condensed phases, gas-phase complexes reveal intrinsic character, such as O_{yl} reactivity, unperturbed by solvent or lattice.[5] Whereas hydration/hydrolysis of solid UO_3 is an inherently complex phenomenon, the analogous bimolecular association of UO_3 and H_2O is relatively straightforward, yielding a discrete hydrate, $UO_3(H_2O)$, or hydroxide, $UO_2(OH)_2$. The reaction of gas-phase UO_3 and H_2O has not been directly examined, but the enthalpy to form $UO_2(OH)_2$ by this process is assigned as -239±3 kJ/mol from high-temperature equilibria, and assuming the hydrate does not remain intact under the experimental conditions.[40-42] As an alternative to investigating hydrolysis of bare neutral UO_3, complexes of UO_3 coordinated by nitrate anions provide a net charge that can be employed for manipulation and detection using electric and magnetic fields. Nitrate ligands furthermore support formation of new metal-oxygen bonds upon elimination of NO_2 by collision induced dissociation (CID), such as in reactions (1a) and (1b). In these reactions the initial metal oxidation state is Y, with no change to oxidation state in reaction (1a) where an $M\text{-}O^{\bullet}$ oxyl bond is formed, but an increase in oxidation state to $Y+1$ in reaction (1b) with formation of a M=O oxo bond. Such nitrate dissociation has been employed to assess a variety of metal oxidation states,[43, 44] including stabilities of +III versus +IV for several f-elements,[45] and the +V state of Pr, Cm, Bk and Cf.[46, 47]

(1a) $[M^{Y+}(NO_3)_{Y+1}]^- \rightarrow [M^{Y+}(O^{\bullet})(NO_3)_Y]^- + NO_2$
(1b) $[M^{Y+}(NO_3)_{Y+1}]^- \rightarrow [M^{(Y+1)+}(O)(NO_3)_Y]^- + NO_2$

Electrospray ionization (ESI) of uranyl nitrate has been shown to generate various gas-phase uranium complexes, including species ***A-D*** in Table 1,[48] which are interrelated by reactions (2)-(4). A focus of the present work was characterization of these species and reactions, with considered isomers in Table 1:

(2) $\boldsymbol{A} \rightarrow \boldsymbol{B} + NO_2$
(3) $\boldsymbol{B} \rightarrow \boldsymbol{C} + NO_3$
(4) $\boldsymbol{C} + H_2O \rightarrow \boldsymbol{D}$

Isomers ***A1***, ***B1***, ***C1*** and ***D1*** are uranyl coordinated by nitrate and: oxyl $O^{\bullet -}$ in ***B1***; oxo O^{2-} in ***C1***; or hydroxo OH^- in ***D1***. In both ***B2*** and ***C2*** a nitrate is replaced by nitrite, with the liberated O combining with oxyl $O^{\bullet -}$ to yield superoxide O_2^- in ***B2***, or with oxo O^{2-} to yield peroxide O_2^{2-} in ***C2***. Isomer ***D2*** is the hydrate alternative to hydroxide ***D1***.

Isomers ***A1*** and ***B1*** were previously established as actual structures of ***A*** and ***B*** by Groenewold et al.[49] The serial CID pathways of $[UO_2(NO_3)_3]^-$ and related species, and the relative energies of rearrangement and fragmentation reactions, were recently revisited in greater detail.[50] A primary goal of the present work was to employ infrared multiple-photon dissociation (IRMPD) spectroscopy, in conjunction with density functional theory (DFT), to assess the structures of ***C*** and ***D***, which resulted in identification of isomers ***C1*** and ***D1***. The particular importance of the present work is that it provides important experimental benchmarks to confirm CID pathways, and for interpretation of vibrational frequencies for specific equatorial ligands. Given the assignment of specific isomer structures, the specifically observed reactions are (2′)-(4′), which correspond to the following transformations of the nitrate-coordinated moieties: UO_2^{2+} (***A1***) → UO_3^+ (***B1***) → UO_3 (***C1***) → $UO_2(OH)_2$ (***D1***). Measured red-shifts for the uranyl asymmetric stretch frequency ν_3 reveal relative donor ligand strengths as greatest for oxo O^{2-} in ***C1***, intermediate for oxyl $O^{\bullet -}$ in ***B1*** and hydroxyl OH^- in ***D1***, and least for nitrate NO_3^- in ***A1***. Hydrolysis reaction (4) reveals activation of the equatorial oxo, $U{=}O_{eq}$, in contrast to the inert axial oxos, $U{=}O_{yl}$.

(2′) ***A1*** → ***B1*** + NO_2
(3′) ***B1*** → ***C1*** + NO_3
(4′) ***C1*** + H_2O → ***D1***

Experimental Methods

CID and Reactivity

Experiments were performed using an Agilent 6340 quadrupole ion trap mass spectrometer (QIT/MS) with a standard ESI source located inside a radiological containment glovebox as described elsewhere.[51] Complex ***A***, $UO_{11}N_3^-$, was produced by ESI of ~100 μM $UO_2(NO_3)_2$ dissolved in ethanol (<10% water). Anion complexes were isolated and subjected to low-energy CID conditions involving multiple energetic collisions between the ions and helium to induce dissociation. The applied CID voltage is an instrumental parameter that was adjusted for different species to provide substantial dissociation while retaining a significant fraction of the undissociated precursor complex. The background H_2O pressure in the ion trap is estimated as $\sim 10^{-6}$ Torr, while the He buffer gas pressure is constant at $\sim 10^{-4}$ Torr.[52] Ion-molecule reactions of CID products with background water are observed if exothermic and kinetically favorable. Anion mass spectra were acquired using the following parameters: ESI flow rate, 60 $\mu L\ min^{-1}$; nebulizer gas pressure,13 psi; capillary voltage, 4800 V; end plate voltage offset, −500 V; dry gas flow rate, 5 L/min; dry gas temperature, 325 °C; capillary exit, −112.5 V; skimmer,−46.2 V; octopole 1 and 2, −12.0 and −1.60 V; octopole RF amplitude, 183.3 Vpp; lens 1 and 2, 8.3 and 94.0 V; trap drive, 63.9.

IRMPD Spectroscopy

The IRMPD experiments employed a Bruker AmaZon Speed ETD QIT/MS at the Free Electron Laser for Infrared eXperiments (FELIX) Laboratory, using procedures described previously.[53, 54] The characteristics of this QIT/MS are generally similar to that used for reactivity studies described above. Complex ***A*** was generated by ESI as described above, complexes ***B*** and ***C*** were produced by CID as reported below, and complex ***D*** was formed by association of complex ***C*** with background water in the ion trap. IRMPD action spectra of complexes ***B***, ***C*** and ***D*** were acquired by monitoring frequency-dependent photodissociation of a mass-selected ion. To accomplish photodissociation, the QIT/MS has been modified such that the high-intensity tunable FELIX infrared beam can be directed into the ion packet, resulting in appreciable multiple-photon dissociation when the laser frequency is in resonance with an adequately intense vibrational mode of the mass-selected complex. IRMPD spectra were generated by plotting the quantity $-\ln\left[\frac{\text{precursor}}{\text{fragments} + \text{precursor}}\right]$, corrected linearly for variations in laser power, as a function of IR wavenumber.[55] The laser produces infrared macropulses having a typical energy of ~40 mJ and a total duration of ~5 μs and are comprised of a sequence of ~1 ps micropulses at 1 GHz. For the experiments reported here, the laser wavelength was tuned in the approximate range 5.9 - 17 μm.

Computational Methods

The potential energy surfaces of all the complexes under study were explored at a scalar-relativistic density functional theory (DFT) level. We have selected the widely used B3LYP hybrid functional[56] because it gives very good agreement between the IRMPD spectrum and the vibrational spectrum calculated for the ***A1*** complex. Note that the description of the electronic structures of actinide complexes with hybrid exchange-correlation functionals usually provides a significant improvement over pure DFT functionals, and that B3LYP was already found to be quite accurate in the work of Groenewold et al.,[49] and the work of Bubas et al.,[50] both of which considered some of the same complexes as in the present study. For the U atom, the small-core scalar-relativistic ECP60MWB energy-consistent pseudopotential[57] was used to mimic the role of the core electrons of the U center and implicitly account for scalar-relativistic effects, together with the (14s13p10d8f6g)/[10s9p5d4f3g] contracted basis set.[58] For the other atoms, all-electron Triple-Zeta-Valence basis sets with Polarization and Diffuse basis functions were used:[59, 60] def2-TZVPD, *i.e.* (12s7p3d1f)/[6s4p3d1f], for O and N, *i.e.* (5s2p)/[3s2p], for H. The relative energies of all the optimized species and the IR linear absorption frequencies were obtained at the same level. All calculations were performed using the Gaussian 09 program package.[61] The infrared absorption spectra, covering the whole experimental spectral range from 600 to 1700 cm^{-1}, were simulated from calculated harmonic frequencies with a scaling factor of 0.978 (derived by best matching the computed and experimental spectra of the ***A1*** species). The calculated frequencies and intensities were convoluted assuming a Lorentzian profile with a full width at half maximum of 15 cm^{-1}.

Results and Discussion

Observed Reactions

Negative ion mode ESI of uranyl nitrate solution produced an abundance of complex ***A***, $UO_{11}N_3^-$ (m/z = 456; ESI mass spectrum shown in Figure S1). Complex ***A*** was isolated and subjected to CID to provide the mass spectrum shown in Figure 1a, where the primary process is reaction (2), elimination of NO_2 from ***A*** to yield ***B,*** $UO_9N_2^-$ (m/z = 410). Also apparent in Figure 1a is a minor peak corresponding to ***D***, $UO_7H_2N^-$ (m/z = 366), which evidently results from secondary fragmentation reaction (3), ***B***-to-***C***, UO_6N^- (348 m/z), followed by water-addition reaction (4), ***C***-to-***D***. As ***B*** was produced in sufficient yield to isolate for secondary CID, the sequence, ***B***-to-***C***-to-***D***, was confirmed as shown in Figure 1b: CID of ***B*** produces ***C*** by reaction (3), which then yields ***D*** by association reaction (4). The results in Figure 1 demonstrate CID reactions (2) and (3), and ion-molecule reaction (4). In contrast to water addition to ***C*** apparent in Figure 1, none of the other species resulted in additional peaks that would indicate a similarly facile water addition process.

Identification of Isomers by IRMPD

The CID results in Figure 1 provide evidence for complex compositions but do not directly reveal their structures. Accordingly, IRMPD spectroscopy along with DFT computations were conducted to provide evidence for structural assignments. Predicted isomer structures are summarized in Table 2, with additional details in Figures 2-6 and the SI. For ***D1*** two very similar structures with C_2 and C_s symmetries are separated by 0.7 kJ/mol, with only the lower-energy C_2 conformer explicitly considered as the two are not effectively differentiated by IR spectroscopy.

The computed structure of ***A1***, $[UO_2(NO_3)_3]^-$, is essentially as previously reported,[62] and subsequently confirmed as the actual structure of ***A*** using IRMPD.[49] Evidence was also presented previously that ***B1*** is the structure of ***B***,[49] an assignment substantiated here by the IRMPD spectrum in Figure 2. For all reported DFT spectra a scaling factor of 0.978 is applied and the peaks are broadened to fairly resemble the IRMPD resolution. Although better agreement might be obtained by fine-tuning the DFT scaling factor, such empirical adjustment would not refine the assessments, because the key comparisons between DFT and IRMPD are not for absolute peak frequencies but rather for patterns and peak separations. Clear-cut structural conclusions can thus be made, despite imperfect agreement between the experiment and uniformly scaled harmonic frequency calculations of different putative isomers. Diagnostic spectral features are provided by nitrate (NO_3^-) and nitrite (NO_2^-), which uncoordinated in solid Ne exhibit ν_3 vibrational modes at 1356.2 cm^{-1} and 1241.5 cm^{-1}, respectively.[63] Upon coordination, the nitrate ν_3 band splits into a low-frequency ν_{3A} and a high-frequency ν_{3B}, for $NaNO_3$ at 1336 cm^{-1} and 1440 cm^{-1}, respectively.[64] In Figure 2, the large predicted ν_{3A}/ν_{3B} splitting for ***B1*** of 235 cm^{-1} is in reasonable accord with the even larger difference of 250 cm^{-1} between the IRMPD peaks at 1262/1512 cm^{-1}. Similar ν_{3A}/ν_{3B} nitrate features are expected for both ***B1*** and ***B2***; these nitrate features thus do not distinguish between these isomers. Instead, ***B1*** is assigned based on the absence of a peak for the nitrite ν_3 mode of ***B2***, ~50 cm^{-1} below the nitrate ν_{3A} peak. The IRMPD results in Figure 2 indicate nitrate, as appears in both isomers ***B1*** and ***B2***, but not nitrite as in ***B2***.

The IRMPD spectrum for ***C*** is shown in Figure 3, along with computed spectra for ***C1*** and ***C2***. As for ***B***, the spectrum exhibits peaks characteristic of nitrate modes ν_{3A} and ν_{3B}, as expected for ***C1*** but not ***C2***. Furthermore, the absence of a nitrite ν_3 peak at lower frequency than nitrate ν_{3A} suggests no significant contribution from isomer ***C2***. The two IRMPD peaks at lower energies are assigned to the ν_2 and ν_4 modes of the UO_3 moiety in ***C1.***[14] The intense peak around 860 cm^{-1} predicted for the uranyl ν_3 mode of ***C2*** is absent. The IRMPD peaks in Figure 3 assigned to nitrate and UO_3 support ***C1*** as the actual structure.

In contrast to the isomers considered for ***B*** and ***C***, isomers ***D1*** and ***D2*** are not differentiated by a nitrite ligand, so other spectral features in Figure 4 must be invoked. The predicted nitrate ν_{3A} and ν_{3B} modes are at essentially the same frequencies for ***D1*** and ***D2***, with these modes for both isomers in accord with the IRMPD peaks at 1273 cm^{-1} and 1486 cm^{-1}. The small IRMPD peak at 1022 cm^{-1} is assigned to the corresponding nitrate ν_1 mode, red-shifted from 1062 cm^{-1} in solid Ne.[63] Isomers ***D1*** and ***D2*** are distinguished by the typical uranyl UO_2^{2+} moiety in ***D1*** that contrasts with the distinctive UO_3 moiety, "uranyl oxide", in ***D2***. The IRMPD peak at 902 cm^{-1} is assigned to the uranyl ν_3 mode of ***D1***. The UO_3 ν_4 mode of ***D2***, which essentially corresponds to a particular case of uranyl ν_3,[14] would have appeared ~70 cm^{-1} lower. It is not the absolute agreement of the scaled DFT and observed uranyl ν_3 that supports ***D1*** over ***D2***, but rather the overall patterns and the frequency of ν_3 *relative* to nitrate peaks. In essence, nitrate provides an internal calibration to confidently assign the peak at 902 cm^{-1} to ***D1*** rather than ***D2***.

Character of the Complexes and Donors

Having identified the structures of the complexes using IRMPD, additional computational results are considered, with emphasis on the actual isomers ***A1***, ***B1***, ***C1*** and ***D1***. Computed structures of all seven isomers are in Figures 5 and 6, along with selected bond distances and angles. All structures are a core linear or quasi-linear uranyl moiety, $O_{yl}=U=O_{yl}$, coordinated by equatorial ligands, with each structure shown in the figures from both side-on and top-down perspectives with respect to the uranyl moiety. Isomer ***A1*** is a linear uranyl coordinated by three bidentate nitrates, as reported previously.[49, 50] In ***B1***, a slightly bent uranyl is coordinated by two nitrates and an oxyl, $O^{\bullet-}$. The identity of the oxyl ligand is established by the spin on ***B1***, $M_S = ½$, essentially concentrated on the equatorial oxygen atom considering Mulliken or Hirshfeld spin densities, which indicates a radical $O^{\bullet}$. The oxyl character is also indicated by a $U-O_{eq}$ single bond distance of 2.127 Å, which is much longer than the $U=O_{yl}$ distance of 1.780 Å, but is close to the U-OH distance of 2.188 Å in ***D1***. In ***B2***, a barely bent uranyl is coordinated by a nitrate, a nitrite, and an O_2 with an O-O distance of 1.306 Å characteristic of superoxide O_2^-.[65] The highly bent uranyl in ***C1*** is coordinated by a nitrate and oxo, O^{2-}. This assignment as an oxo in a UO_3 moiety is established by net zero spin associated with hexavalent uranium and saturated oxygens; and by a $U-O_{eq}$ double bond distance of 1.881 Å that is only slightly longer than $U=O_{yl}$, 1.827 Å, and much shorter than both $U-O^{\bullet}_{eq}$ in ***B1*** (2.127 Å) and U-OH in ***D1*** (2.188 Å). The uranyl in ***C2*** is also highly bent, with coordination by a nitrite and an O_2 with O-O distance 1.435 Å corresponding to peroxide O_2^{2-}.[65] The slightly bent uranyl in ***D1*** is coordinated by a nitrate and two hydroxyls. Finally, ***D2*** is essentially similar to ***C1*** but with addition of an equatorial H_2O exhibiting a long $U-O_{H2O}$ dative bond distance of 2.780 Å.

As suggested above, and by inclusion in Table 2 of the UO_3 ν_4 mode for isomer ***C1***, this mode essentially corresponds to the uranyl ν_3 stretching mode, as discussed by Gabelnick et al.[14] The ν_4 mode appears at 853 cm^{-1} for UO_3 trapped in solid argon[14] and is shifted to 801 cm^{-1} in ***C1***. For bare UO_2^{2+}, ν_3 has been estimated as ~1110 cm^{-1},[5] which red-shifts to lower energies as the uranyl bonds are weakened due to increasing number and/or efficacy of equatorial donors.[5, 7, 49, 66] The three nitrates in ***A1*** induce a large red-shift in ν_3, to 949 cm^{-1}.[49] For ***D1*** there is a further red-shift to 905 cm^{-1}, coincident with $U=O_{yl}$ bond elongation and slight uranyl bending. As two nitrates in ***A1*** are replaced by hydroxides in ***D1***, weakening of the uranyl bonds from ***A1*** to ***D1*** reveals hydroxide as a better donor than nitrate,[67] a relationship similarly established in solution based on the Raman active uranyl ν_2 mode.[68] The result of comparable uranyl ν_3 frequencies for ***B1*** and ***D1***, respectively 896 cm^{-1} and 905 cm^{-1}, suggests similar donor efficacy for one $O^{\bullet-}$ in ***B1*** and two OH^-

in ***D1***. The implication that oxyl is a better donor than hydroxyl is supported by shorter bond distances for U-O$^{\bullet}$ versus U-OH.

In contrast to familiar anions like nitrate and hydroxide, efficacies of donors oxyl and oxo, which appear in ***B1*** and ***C1***, respectively, are less commonly directly compared. From the structures in Figures 5 and 6, and properties in Table 2, it is apparent that ***B1*** is a characteristic uranyl complex, essentially similar to ***A1*** and ***D1*** but with an oxyl as one of the three equatorial ligands. In contrast, the structure of ***C1*** exhibits substantial divergence from a typical uranyl, including a very bent uranyl angle of 160º, long U=O_{yl} distances of 1.83 Å, and an extreme red-shift of ν_4—surrogate for uranyl ν_3—to 801 cm^{-1}. Another distinctive feature of the structure of ***C1*** in Figure 6 is excessive crowding of the equatorial oxo and nitrate ligands towards the same side of the equatorial plane, a situation that induces a substantial uranyl bend in the opposite direction. This highly non-symmetrical equatorial coordination suggests orbital-oriented covalent ligand bonding, analogous to that which induces the characteristic structure of uranyl.[23, 67] Greater disruption of the uranyl moiety in ***C1*** versus ***B1*** reveals that the oxo and nitrate in ***C1*** are more effective donors than the oxyl and two nitrates in ***B1***. It is thus evident that oxo is a very strong donor, significantly stronger than oxyl. The following overall order of donor ligand efficacy is established by the present results: *oxo* O_2^{2-} *>> oxyl* $O^{\bullet -}$ *> hydroxide* OH^- *> nitrate* NO_3^-.

Just as variations in uranyl characteristics like distances and vibrational frequencies reveal disruption to its bonding, a ligand such as nitrate is similarly disturbed upon coordination. Bare nitrate has C_{3v} symmetry, with only slight deviation from planarity, and an IR-active fundamental asymmetric stretch mode ν_3, which appears at 1356 cm^{-1} for NO_3^- in solid neon.[63] Coordination of nitrate breaks the D_{3h} symmetry, with resultant splitting of ν_3 into ν_{3A} and ν_{3B},[64] a characteristic invoked above to interpret the IRMPD results. It has been shown that the magnitude of the nitrate ν_3 splitting, $\Delta[\nu_{3B}$-$\nu_{3A}]$, parallels the extent of bonding to the substrate.[64] Another indicator of nitrate disruption, and thus substrate bonding, is the angle ∠O-N-O defined by the two nitrate O atoms coordinated to a metal. Nitrate parameters in Table 3 show that $\Delta[\nu_{3B}$-$\nu_{3A}]$, and the contraction of ∠O-N-O relative to the free nitrate angle of 120º, vary in concert in the following order: ***A1*** *[most distorted nitrate]* > ***B1*** > ***D1*** > ***C1***. This is the same sequence as for equatorial coordination number, possibly reflecting increased nitrate distortion due to repulsion between ligands. However, inter-ligand repulsion is evidently not the only pertinent effect as the uranyl-nitrate bond distances (Table 2) show a similar trend: ***A1*** *[shortest/strongest U-*O_{NO3} *bonds]* > ***B1*** > ***D1*** ≈ ***C1***. As noted above, the uranyl ν_3 red-shift indicates a very different order for overall equatorial bonding: ***C1*** *[most equatorial bonding]* > ***B1*** > ***D1*** > ***A1***. The result that nitrate is most deformed and strongly bound to uranyl in ***A1***, coincident with the least overall equatorial binding, and vice versa for ***C1***, indicates that variations in aggregate equatorial bonding are dominated by other better donor ligands, specifically by oxo, oxyl and hydroxyl.

Energies of Isomers and Reactions

As indicated in Table 2, ***B1*** and ***B2*** are at practically the same energy, with a difference of 3.0 kJ/mol that lies within computational uncertainty. However, the IRMPD results in Figure 2 show that only isomer ***B1*** results from reaction (2), which may reflect a kinetic barrier to formation of ***B2***. Referring to Figure 5, transformation ***A1→B1*** corresponds to simple cleavage of an O-NO_2 bond, with the NO_2 fragment ejected and the liberated O remaining bound to U. Non-observed process ***A1→ B2*** similarly requires O-NO_2 cleavage and NO_2 elimination, but in this case the liberated O must associate with an O from another NO_3 to yield bound O_2 and NO_2. The greater kinetic barrier to form ***B2*** versus ***B1*** is consistent with the observed dominance of the latter. We note that the energetics for decomposition of ***A1*** were recently investigated independently,[50] and the transition state for isomerization of ***A1*** to lead to isomer ***B2*** was found to be significantly higher than the energy required for direct formation of B1 by ejection of NO_2. The current computed energies, combined with those from previous studies, conclusively show that the formation of ***B2*** by rearrangement of ***A1*** is not competitive.

In contrast to energetically similar ***B1*** and ***B2***, isomer ***C1*** is predicted to be 103 kJ/mol lower than ***C2***. In addition to transformation ***B1→C1*** being energetically favored, the structures in Figures 5 and 6 suggest it should be relatively facile as it corresponds to elimination of an intact NO_3 concomitant with electron transfer to reduce oxyl $O^{\bullet -}$ to oxo O^{2-}. Alternative transformation ***B1→C2*** to produce NO_2 and O_2 ligands requires intramolecular O-atom transfer from NO_3 to O. Observation of only ***C1*** is thus consistent with both thermodynamic and kinetic considerations.

For ***D1***, the energy difference is only 0.7 kJ/mol between symmetry C_2 and C_S conformers with respective *trans* and *cis* hydroxide orientation. These conformers are predicted to exhibit such similar vibrational features that they are not effectively differentiated by IRMPD spectroscopy. The species identified as ***D1*** may thus be conformer C_2 or C_S, or more likely a mixture of the two at the ion trap temperature of ~300 K.[69] Hydrate isomer ***D2*** is computed as 117 kJ/mol higher in energy than hydroxide ***D1***. Isomer ***D2*** is formed from ***C1*** by straightforward association of H_2O. In contrast, formation of ***D1*** requires H-atom transfer from adsorbed H_2O to an equatorial oxo ligand. The lower-energy but kinetically more demanding hydroxide isomer ***D1*** was assigned above based on IRMPD (Figure 4).

Nitrate dissociation reactions (2′) and (3′) are computed as endothermic by 264 kJ/mol and 245 kJ/mol, respectively, which are energies consistent with an independent investigation of fragmentation energetics of uranyl nitrate anions[50] and are in a range previously shown accessible under comparable CID conditions.[70] Hydrolysis reaction (4′), computed as exothermic by -175 kJ/mol, is pertinent to reactions of solid UO_3 with water. In the present study, alternative hydration to produce ***D2*** is computed as exothermic by only -58 kJ/mol, which may be an insufficient energy for the hydrate to remain bound in the ion trap at ~300 K.[52, 69] An earlier investigation[50] of the reaction mechanism revealed a similar result, and placed the free energy for proton transfer to create the dihydroxide ~12 kJ/mol above ***D2***, and ~7 kJ/mol below the energy of ***C1***+H_2O. The computed energy of reaction (4′) is much less negative than $\Delta H^{298} = -239$ kJ/mol reported for hydrolysis of bare uranium trioxide—$UO_3 + H_2O \rightarrow UO_2(OH)_2$.[42] The disparity is even larger relative to $\Delta H^{298} = -171$ kJ/mol for reaction (4′). The disparity between the bare and ligated complexes may reflect weaker U-OH bonds in ***D1*** due to donors reducing the positive charge on uranium. For both bare UO_3 and ***C1***, as for solid UO_3, hydrolysis is thermodynamically favored relative to hydration. This propensity for hydrolysis is characteristic of the equatorial oxo and contrasts with most uranyl compounds, such as inert uranyl nitrate.[71]

Distinctive hydrolysis of the equatorial oxo in ***C1*** captures a fundamental characteristic of uranium trioxide chemistry. In Figure 1b no peak is apparent at 384 m/z, which would correspond to addition of another H_2O to ***D1*** by hydrolysis of a uranyl oxo bond. It is well established that $U{=}O_{yl}$ bonds are generally resistant to such activation.[72] The inert character of the uranyl moiety, particularly towards hydrolysis, is reflected in the prediction that hydrate $[UO_2(H_2O)]^{2+}$ is 94 kJ/mol lower in energy than hydroxide $[UO(OH)_2]^{2+}$.[73] The contrasting character of the hydrolysable equatorial oxo versus inert axial oxos in uranyl complex ***C1*** reveals the essential nature of the constituent UO_3 moiety, as well as that of solid UO_3. Ion-molecule reaction (5) between ***B1*** and toluene was previously reported.[74] Although the oxyl ligand in ***B1*** is resistant to hydrolysis such as occurs for the oxo in reaction (4′), exothermic reaction (5) demonstrates that the oxyl can convert to hydroxide by abstracting a suitably reactive H atom. Whereas reaction (4′) to yield dihydroxide is diagnostic for an equatorial oxo, reactions like (5) to yield monohydroxide serve as diagnostic for oxyl.

$$(5)\quad [UO_2(O^{\bullet})(NO_3)_2]^- \ (\boldsymbol{B1}) + C_6H_5CH_3 \rightarrow [UO_2(OH)(NO_3)_2]^- + C_6H_5CH_2^{\bullet}$$

Conclusions

Transformations and key properties of the complexes derived from reactivity, IRMPD spectroscopy and DFT calculations are summarized in Figure 7. Dissociation of uranyl nitrate ***A1*** ($[UO_2(NO_3)_3]^-$) produces uranyl oxyl nitrate ***B1*** ($[UO_2(O^{\bullet})(NO_3)_2]^-$), followed by uranyl oxo nitrate ***C1*** ($[UO_2(O)(NO_3)]^-$). Exothermic addition of water to ***C1*** results in hydroxide ***D1*** ($[UO_2(OH)_2(NO_3)]^-$). As in bare UO_3, the equatorial $U{=}O_{eq}$ oxo bond in ***C1*** is longer than the axial $U{=}O_{yl}$ oxo bonds; also, the equatorial oxo hydrolyzes to hydroxo, whereas the axial oxos are inert. The equatorial $U\text{-}O^{\bullet}_{eq}$ oxyl bond in ***B1*** is much longer and weaker than oxo bonds, but it does not hydrolyze. In all four complexes, weakening of axial $U{=}O_{yl}$ bonds due to equatorial donors is revealed by red-shifting of the uranyl ν_3 asymmetric stretch, which is particularly pronounced for the "strong but reactive" equatorial oxo in ***C1***. Excessive congestion of the equatorial oxo and nitrate ligands in ***C1*** furthermore suggests significant covalent bonding of the oxo and nitrate ligands. Overall, the uranyl ν_3 frequencies and $U{=}O_{yl}$ distances provide the following order of uranyl bond weakening due to equatorial donors: *oxo* O^{2-} *[most uranyl weakening/strongest donor] >> oxyl* $O^{\bullet -}$ *> hydroxide* OH^- *> nitrate* NO_3^-.

Donor effects indicate $U{=}O_{yl}$ bond weakening with decreasing positive charge on uranium. Plotted in Figure 8 are bond distances for neutral, cationic and anionic UO_3,[25, 75] as well as for nitrate-coordinated UO_3. For the bare trioxides, the $U{=}O_{yl}$ bond is shortest/strongest in UO_3^+, intermediate in UO_3, and longest/weakest in UO_3^-, substantiating the general expectation that lower positive charge on U results in weaker bonds to O. The $U{=}O_{yl}$ distance in ***B1***, lying between those for UO_3^+ and UO_3, supports characterization of ***B1*** as UO_3^+ with the positive charge moderated by the donor nitrates. Similarly, the $U{=}O_{yl}$ distance in ***C1***, between those for UO_3 and UO_3^-, indicates UO_3 with a fractional negative charge. Whereas the $U{=}O_{yl}$ distances in Figure 8 vary gradually, the oxyl U-$O^{\bullet}_{eq}$ bonds in bare cation UO_3^+ and complex ***B1*** are much longer than all of the reported oxo bonds. These correlations between bond distances and charge suggest that weakening of the uranium-oxygen bonds is dominated by electrostatics rather than covalency.

Sensitive gas-phase approaches can elucidate chemistry of scarce and radioactive elements. Experiments reported for transuranium actinide (An) trioxides, AnO_3, are very limited, such as to mere detection of PuO_3.[76] Based on results here, $[AnO_2(O)(NO_3)]^-$ complexes offer a means to reveal essential characteristics of the constituent AnO_3 moiety. Like UO_3, NpO_3 and PuO_3 are predicted to be actinyl(VI) coordinated by an oxo, An=O_{eq}. In contrast, later actinides may instead be actinyl(V) coordinated by an oxyl, An-$O^{\bullet}_{eq}$.[77, 78] These two types of AnO_3 could be differentiated by characteristic reactivity such as demonstrated for UO_3 here and previously,[74] to wit hydrolysis of An=O_{eq} to $An(OH)_2$ versus reduction of An-$O^{\bullet}_{eq}$ to An-OH. Curium, at the middle of the actinide series, is key to understanding earlier and later members. Essential characteristics at this "turning point" appear in the prediction of three CmO_3 isomers/oxidation states within ~35 kJ/mol:[78] oxo superoxide, $Cm^{III}O(O_2)$; oxo peroxide, $Cm^{IV}O(O_2)$; and actinyl(V) oxyl, $Cm^{V}O_2(O^{\bullet})$. Determination of the actual nature of CmO_3 and other key species would provide insights into properties and trends across the actinide series that may not be accessible using conventional bulk-scale synthesis and characterization approaches.

Supporting Information

ESI mass spectrum of uranyl nitrate. Geometrical coordinates and energies for the computed structures.

Acknowledgements

Supported by the U.S. Department of Energy, Office of Basic Energy Sciences, Chemical Sciences, Geosciences, and Biosciences, Heavy Element Chemistry, at LBNL under Contract DE-AC02-05CH11231 (J.J. and J.K.G.). This research used resources of CCIPL ("Centre de Calcul Intensif des Pays de Loire"). We gratefully acknowledge the Nederlandse Organisatie voor Wetenschappelijk Onderzoek (NWO) for the support of the FELIX Laboratory

Table 1. Complex compositions and isomers

Composition		Isomer		Uranyl coordination
A	**$UO_{11}N_3^-$**	***A1***	$[UO_2(NO_3)_3]^-$	Nitrate
B	**$UO_9N_2^-$**	***B1***	$[UO_2(O^{\bullet})(NO_3)_2]^-$	Oxyl & nitrate
		B2	$[UO_2(NO_3)(NO_2)(O_2)]^-$	Nitrate, nitrite & superoxide
C	**UO_6N^-**	***C1***	$[UO_2(O)(NO_3)]^-$	Oxo & nitrate
		C2	$[UO_2(NO_2)(O_2)]^-$	Nitrite & peroxide
D	**$UO_7H_2N^-$**	***D1***	$[UO_2(OH)_2(NO_3)]^-$	Hydroxide & nitrate
		D2	$[UO_2(O)(NO_3)(H_2O)]^-$	Oxo, nitrate & hydrate

Table 2. Isomer energies, frequencies, bond distances and angles.

Isomer (symmetry)	ΔE / *CN_{eq}*[a]	Frequency[b]		Bond distance (Å)[c]			Angle[d]
		IRMPD	DFT	U-O_{yl}	U-O_{eq}	U-O_{NO3}	O_{yl}-U-O_{yl}
A1 (D_{3h}) $[UO_2(NO_3)_3]^-$	GS / *6*	949	924	1.766	-	2.503	180.0°
B1 (C_{2v}) $[UO_2(O^{\bullet})(NO_3)_2]^-$	GS / *5*	896	904	1.780	2.127	2.532	178.9°
B2 (C_s) $[UO_2(NO_3)(NO_2)(O_2)]^-$	3. 0 / *6*	-	922	1.774	2.382	2.526	179.5°
C1 (C_s) $[UO_2(O)(NO_3)]^-$	GS / *3*	801	813	1.827	1.881	2.579	160.0°
C2 (C_s) $[UO_2(NO_2)(O_2)]^-$	103.2 / *4*	-	865	1.800	2.158	-	166.5°
D1 (C_2; C_s) $[UO_2(OH)_2(NO_3)]^-$	GS; 0.7 / *4*	905	895	1.789	2.188	2.576	177.9°
D2 (C_1) $[UO_2(O)(NO_3)(H_2O)]^-$	117.2 / *4*	-	824	1.821	1.918	2.581	164.0°

[a] Energy is relative to ground state in kJ/mol. *CN_{eq}* is the equatorial coordination number.

[b] In cm^{-1} for uranyl ν_3 or UO_3 ν_4 for ***C1***. DFT values are scaled. ***A1*** from Groenewold et al.[49]

[c] O_{eq} is O, O_2 or OH. Average if more than one NO_3 distance.

[d] The uranyl moiety in ***C1***, ***C2*** and ***D2*** is substantially bent away from the equatorial ligands.

Table 3. Nitrate frequencies, bond distances to uranium, and angles.

Isomer		ν_{3A}[a]	ν_{3B}[a]	$\Delta[\nu_{3B}-\nu_{3A}]$[a]	∠O-N-O[b]	d[U-O_{NO3}][c]
A1	$[UO_2(NO_3)_3]^-$	1273	1537	264	114.8°	2.503
B1	$[UO_2(O^\bullet)(NO_3)_2]^-$	1262	1512	250	115.1°	2.532
C1	$[UO_2(O)(NO_3)]^-$	1275	1465	190	116.4°	2.579
D1	$[UO_2(OH)_2(NO_3)]^-$	1273	1486	213	116.1°	2.576

[a] Nitrate ν_3 mode split into ν_{3A} and ν_{3B} as determined experimentally.[63, 64] ***A1*** values are from Groenewold et al.[49]

[b] Angle O-N-O for the two nitrate O atoms coordinated to uranium.

[c] Uranium-nitrate distances (Å); average if more than one distance.

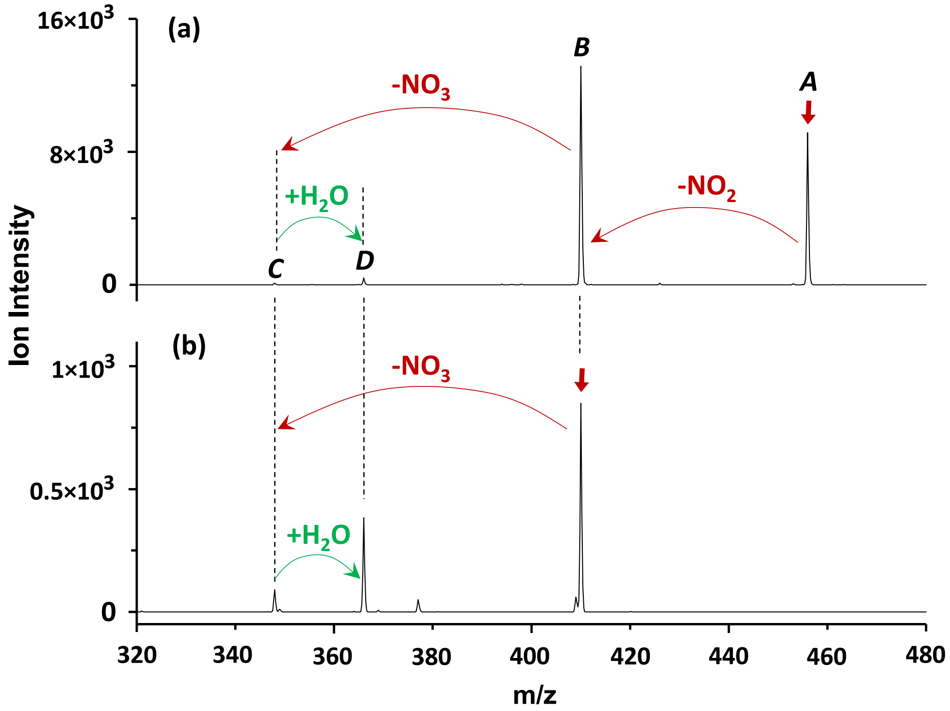

Figure 1. CID mass spectra for (a) complex ***A*** (456 m/z) to yield ***B*** (410 m/z), ***C*** (348 m/z) and ***D*** (366 m/z); and (b) ***B*** to yield ***C***, and ***D*** from reaction with background water (the small unassigned peak in (b) is 377 m/z). Applied CID voltages: (a) 0.35 V; (b) 0.40 V.

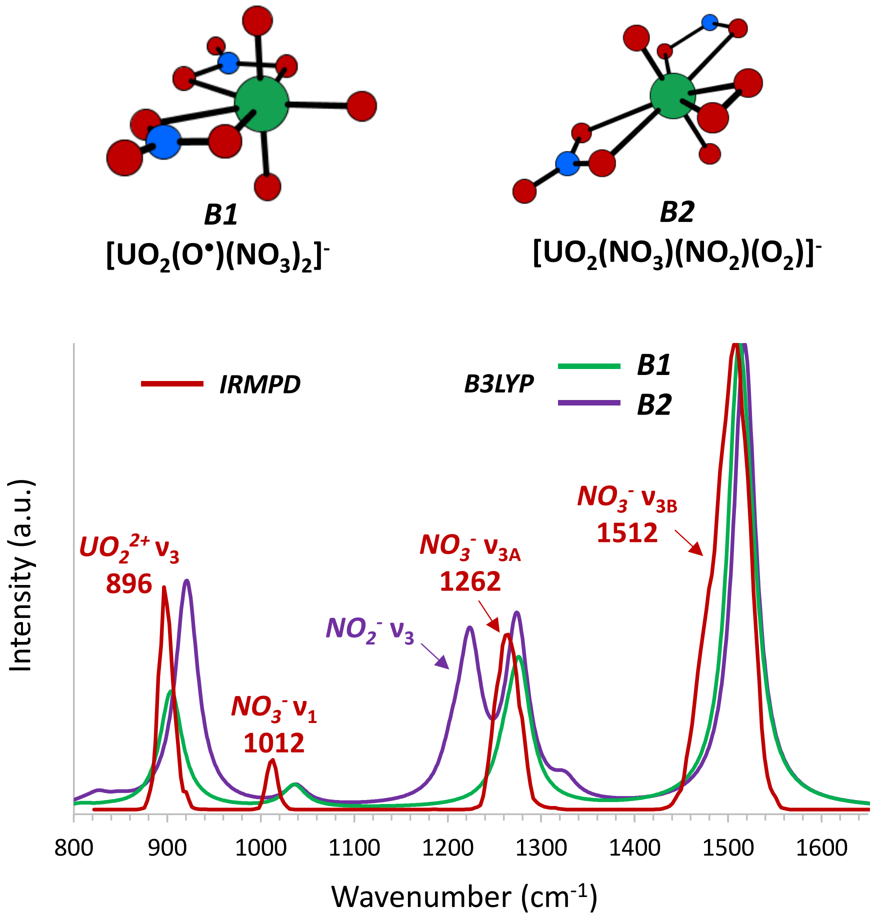

Figure 2. IRMPD spectrum of ***B***, (solid and dashed red) and computed spectra for ***B1*** and ***B2***, with structures at the top (green = U; red = O; blue = N). The IRMPD peaks labeled in red coincide with the predictions for ***B1***. Non-observed nitrite peak for ***B2*** is labeled in purple. The results identify ***B*** as isomer ***B1***.

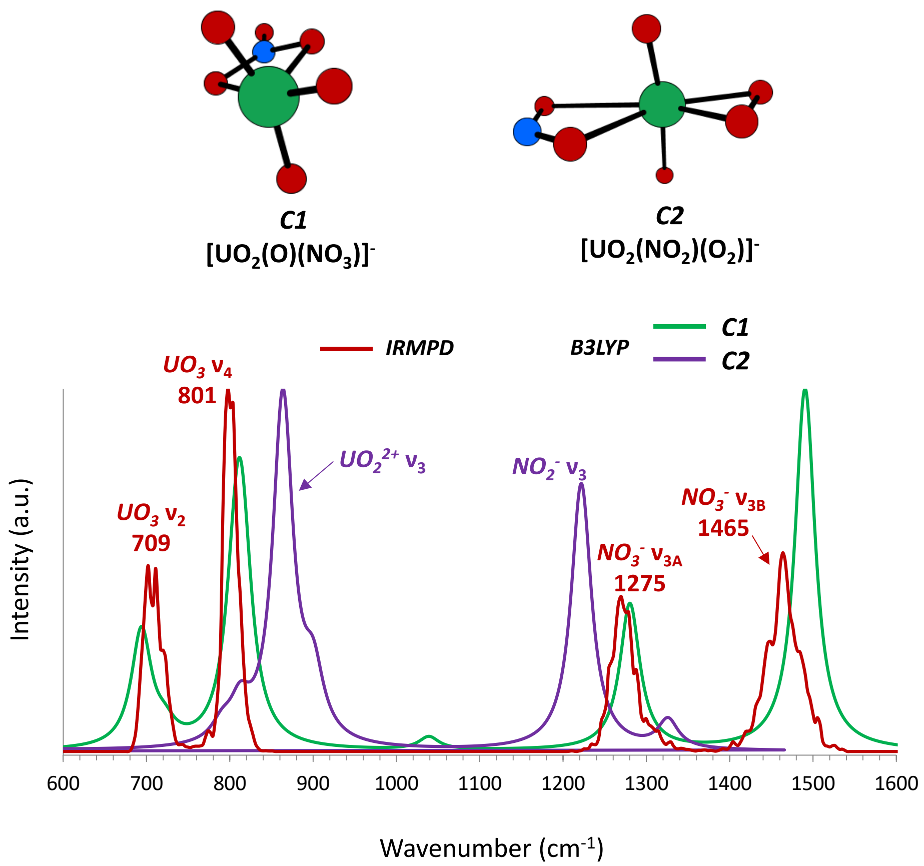

Figure 3. IRMPD spectrum of ***C*** (red) and computed spectra for ***C1*** and ***C2***, with structures at the top (green = U; red = O; blue = N). The IRMPD peaks labeled in red coincide with predictions for ***C1.*** Non-observed peaks for ***C2*** are labeled in purple. The results identify ***C*** as isomer ***C1***.

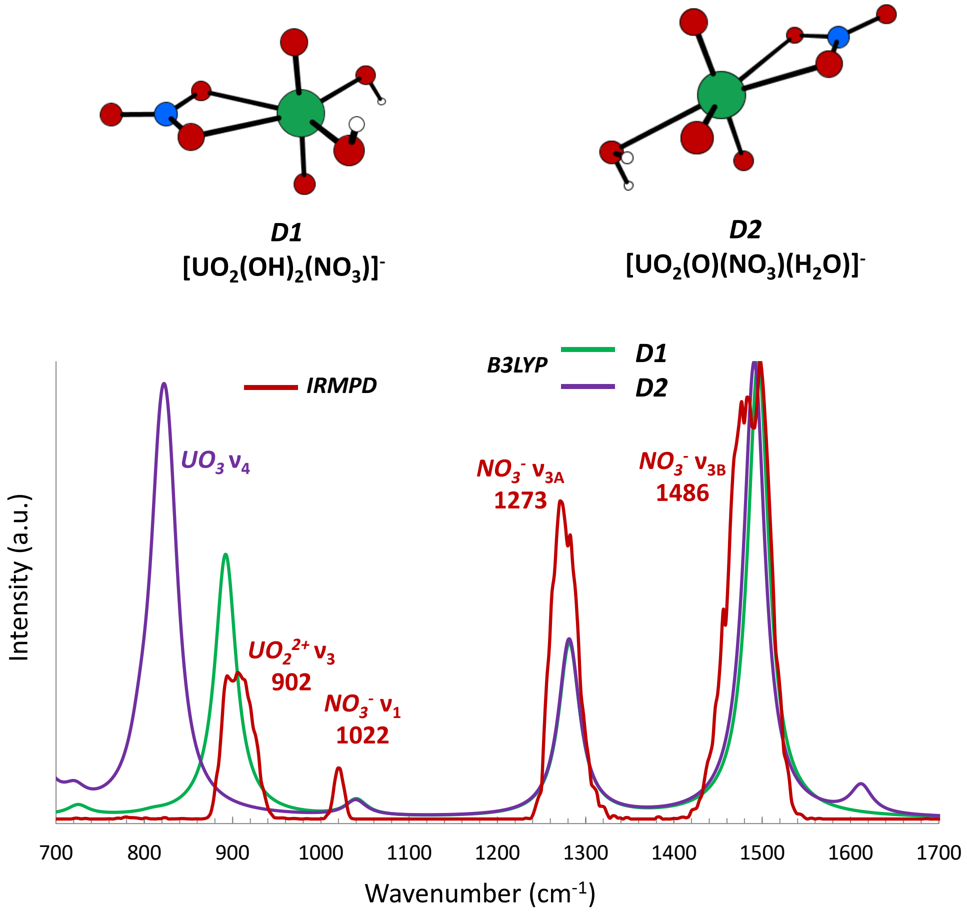

Figure 4. IRMPD spectrum of ***D*** (red) and computed spectra for ***D1*** and ***D2***, with structures at the top (green = U; red = O; blue = N; grey = H). The predicted spectra for D1 and D2 are essentially coincident in the range 980 – 1560 cm^{-1}. The IRMPD peaks labeled in red coincide with predictions for ***D1.*** The non-observed UO$_3$ peak for ***D2*** is labeled in purple. The results identify ***D*** as isomer ***D1***.

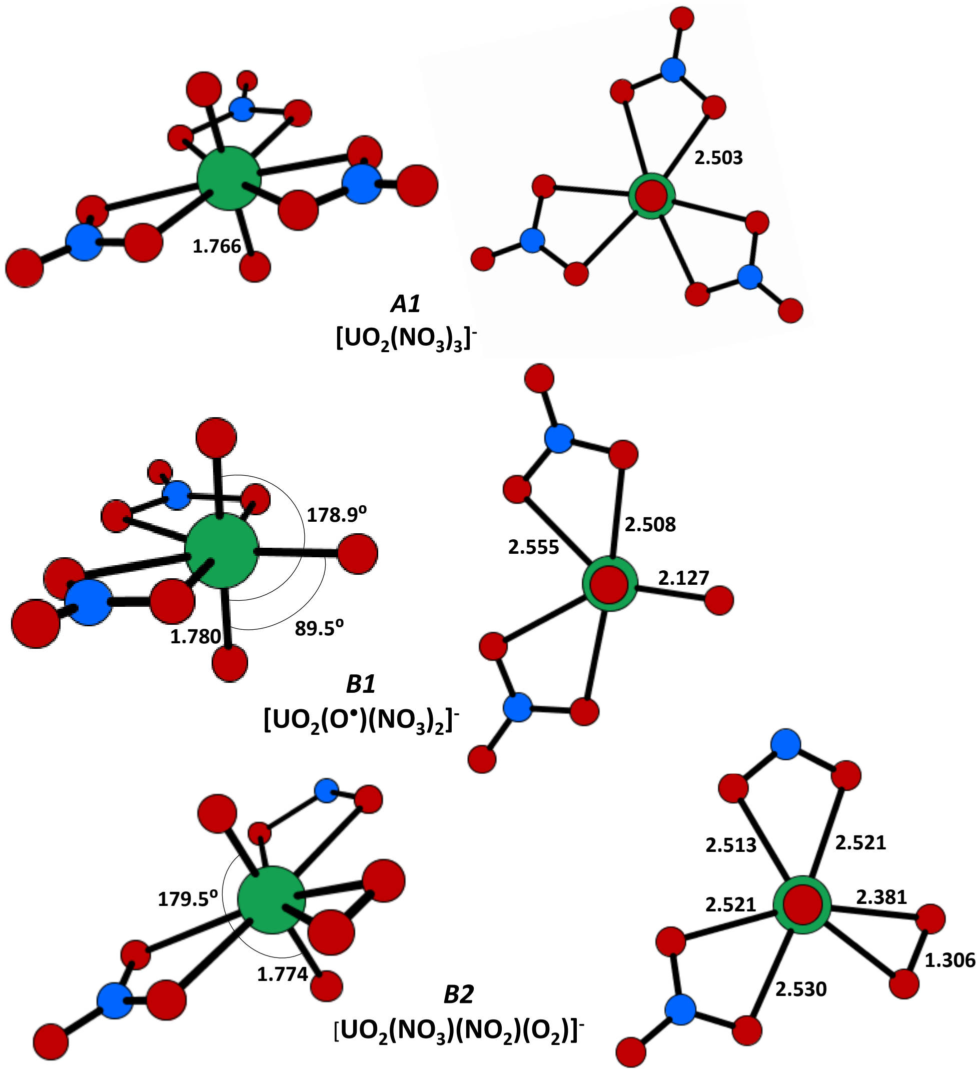

Figure 5. Computed structures ***A1***, ***B1*** and ***B2***, from "side" (left) and "top" (right) perspectives with respect to the uranyl moiety (green = U; red = O; blue = N). Bond distances are Å; angles are degrees.

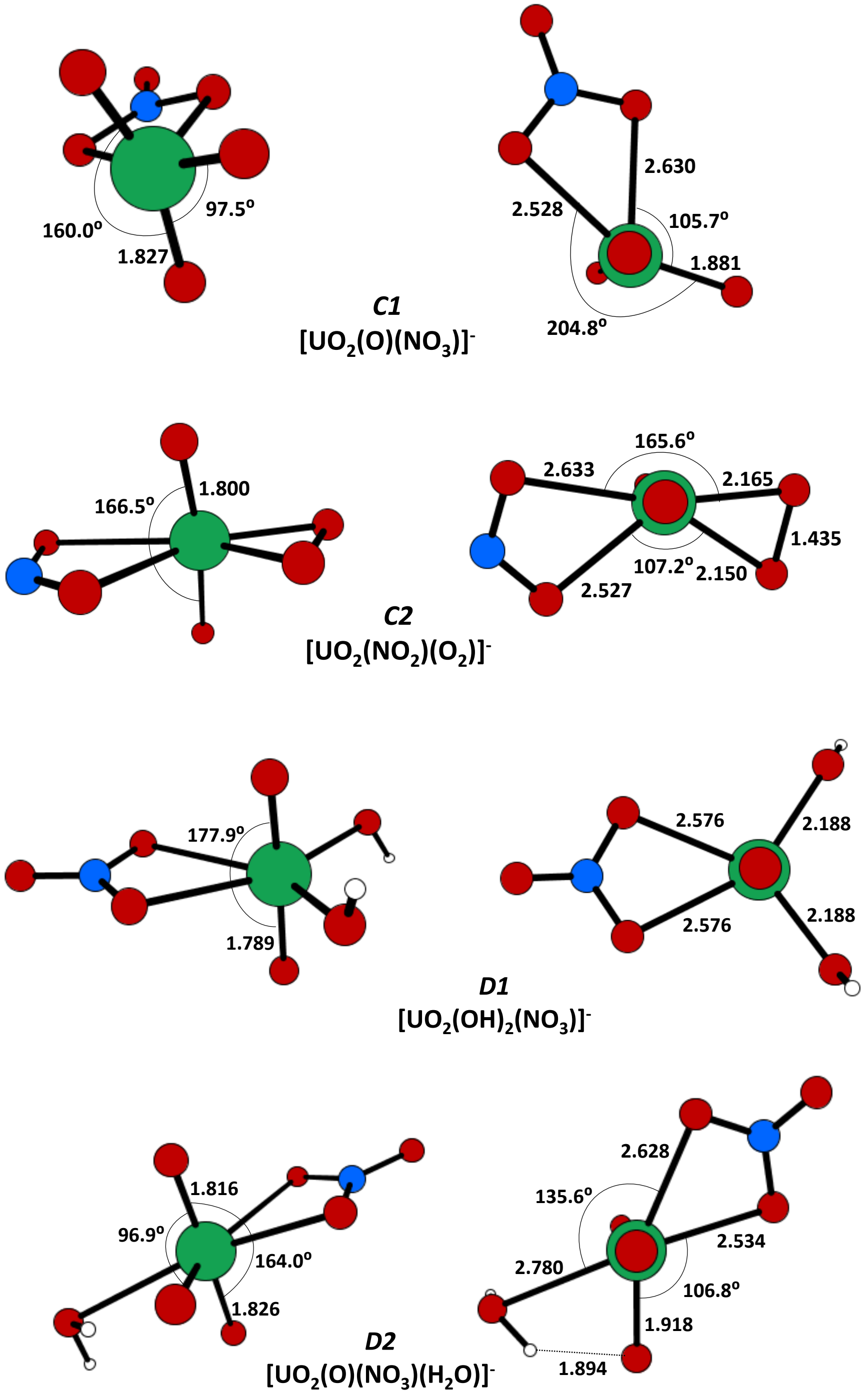

Figure 6. Computed structures ***C1***, ***C2***, ***D1*** and ***D2***, from "side" (left) and "top" (right) perspectives with respect to the uranyl moiety (green = U; red = O; blue = N; grey = H). Bond distances are in Å. For ***D1*** the shown C_2 structure has *trans* OH groups; in the C_S conformer 0.7 kJ/mol higher energy they are *cis*.

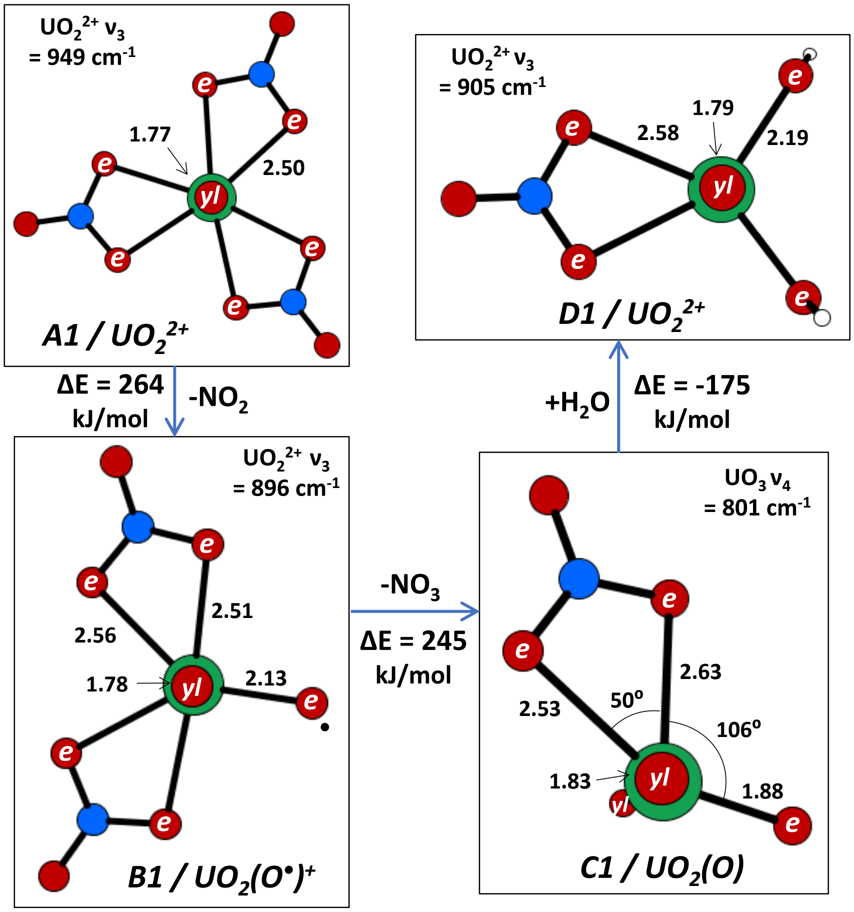

Figure 7. Summary of transformations ***A1***→***B1***→***C1***→***D1***. Structures are viewed parallel to uranyl, O_{yl}=U=O_{yl}, with equatorial (*e*) and axial (*yl*) O atoms indicated. The second O_{yl} in ***C1*** is not fully eclipsed. Distances are Å; angles are degrees. Green = U; red = O; blue = N; grey = H.

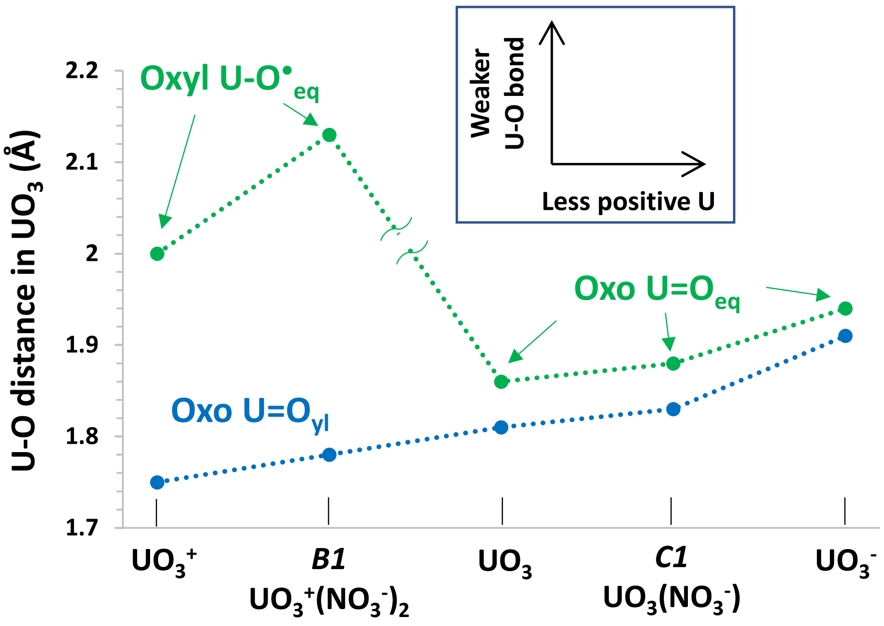

Figure 8. Axial and equatorial uranium-oxygen distances, U-O_{yl} (blue) and U-O_{eq} (green) for UO_3 in different charge states and complexes, computed at comparable theory levels (UO_3 and UO_3^+ from Vasiliu et al.;[25] UO_3^- from Michelini et al.;[75] ***B1*** and ***C1*** from this work).

References

1. Pyykkö, P.; Li, J.; Runeberg, N., Quasi-Relativistic Pseudopotential Study of Species Isoelectronic to Uranyl and the Equatorial Coordination of Uranyl. *J Phys Chem-Us* **1994,** *98* (18), 4809-4813.

2. McGlynn, S. P.; Neely, W. C.; Smith, J. K., Electronic Structure, Spectra, and Magnetic Properties of Oxycations .3. Ligation Effects on Infrared Spectrum of Uranyl Ion. *J Chem Phys* **1961,** *35* (1), 105-116.

3. Tsushima, S., On the "yl" Bond Weakening in Uranyl(VI) Coordination Complexes. *Dalton T* **2011,** *40* (25), 6732-6737.

4. Di Pietro, P.; Kerridge, A., U-O_{yl} Stretching Vibrations as a Quantitative Measure of the Equatorial Bond Covalency in Uranyl Complexes: A Quantum-Chemical Investigation. *Inorg Chem* **2016,** *55* (2), 573-583.

5. Groenewold, G. S.; Gianotto, A. K.; Cossel, K. C.; Van Stipdonk, M. J.; Moore, D. T.; Polfer, N.; Oomens, J.; de Jong, W. A.; Visscher, L., Vibrational Spectroscopy of Mass-Selected $[UO_2(ligand)_n]^{2+}$ Complexes in the Gas Phase: Comparison with Theory. *J Am Chem Soc* **2006,** *128* (14), 4802-4813.

6. Abergel, R. J.; de Jong, W. A.; Deblonde, G. J. P.; Dau, P. D.; Captain, I.; Eaton, T. M.; Jian, J. W.; van Stipdonk, M. J.; Martens, J.; Berden, G., et al., Cleaving Off Uranyl Oxygens through Chelation: A Mechanistic Study in the Gas Phase. *Inorg Chem* **2017,** *56* (21), 12930-12937.

7. Gibson, J. K.; de Jong, W. A.; van Stipdonk, M. J.; Martens, J.; Berden, G.; Oomens, J., Equatorial Coordination of Uranyl: Correlating Ligand Charge Donation with the O_{yl}-U-O_{yl} Asymmetric Stretch Frequency. *J Organomet Chem* **2018,** *857*, 94-100.

8. Conn, G. K. T.; Wu, C. K., An Investigation of the Raman and Infrared Spectra of Certain Uranyl Salts, with Conclusions on the Structure of the Uranyl Group. *T Faraday Soc* **1938,** *34* (2), 1483-1491.

9. Jones, L. H., Systematics in the Vibrational Spectra of Uranyl Complexes. *Spectrochim Acta* **1958,** *10* (4), 395-403.

10. Bell, N. L.; Shaw, B.; Arnold, P. L.; Love, J. B., Uranyl to Uranium(IV) Conversion through Manipulation of Axial and Equatorial Ligands. *J Am Chem Soc* **2018,** *140* (9), 3378-3384.

11. Clark, D. L.; Conradson, S. D.; Donohoe, R. J.; Keogh, D. W.; Morris, D. E.; Palmer, P. D.; Rogers, R. D.; Tait, C. D., Chemical Speciation of the Uranyl Ion Under Highly Alkaline Conditions. Synthesis, Structures, and Oxo Ligand Exchange Dynamics. *Inorg Chem* **1999,** *38* (7), 1456-1466.

12. Alexander, C. A., Volatilization of Urania Under Strongly Oxidizing Conditions. *J Nucl Mater* **2005,** *346* (2-3), 312-318.

13. Koroglu, B.; Dai, Z. R.; Finko, M.; Armstrong, M. R.; Crowhurst, J. C.; Curreli, D.; Weisz, D. G.; Radousky, H. B.; Knight, K. B.; Rose, T. P., Experimental Investigation of Uranium Volatility during Vapor Condensation. *Anal Chem* **2020,** *92* (9), 6437-6445.

14. Gabelnick, S. D.; Reedy, G. T.; Chasanov, M. G., Infrared-Spectra of Matrix-Isolated Uranium Oxide Species .2. Spectral Interpretation and Structure of UO_3. *J Chem Phys* **1973,** *59* (12), 6397-6404.

15. Green, D. W.; Reedy, G. T.; Gabelnick, S. D., Infrared Spectra of Matrix-Isolated Uranium Oxides .3. Low-Frequency Modes. *J Chem Phys* **1980,** *73* (9), 4207-4216.

16. Hunt, R. D.; Andrews, L., Reactions of Pulsed-Laser Evaporated Uranium Atoms with Molecular-Oxygen - Infrared-Spectra of UO, UO_2, UO_3, UO_2^+, UO_2^{2+}, and UO_3-O_2 in Solid Argon. *J Chem Phys* **1993,** *98* (5), 3690-3696.

17. Kovács, A.; Konings, R. J. M.; Gibson, J. K.; Infante, I.; Gagliardi, L., Quantum Chemical Calculations and Experimental Investigations of Molecular Actinide Oxides. *Chem Rev* **2015,** *115* (4), 1725-1759.

18. Zhou, M. F.; Andrews, L.; Ismail, N.; Marsden, C., Infrared Spectra of UO_2, UO_2^+, and UO_2^- in Solid Neon. *J Phys Chem A* **2000,** *104* (23), 5495-5502.

19. Uzunova, E. L., Electronic Structure of Trioxide, Oxoperoxide, Oxosuperoxide, and Ozonide Clusters of the 3d Elements: Density Functional Theory Study. *J Phys Chem A* **2011,** *115* (8), 1320-1330.

20. Li, S. G.; Dixon, D. A., Molecular and Electronic Structures, Bronsted Basicities, and Lewis Acidities of Group VIB Transition Metal Oxide Clusters. *J Phys Chem A* **2006,** *110* (19), 6231-6244.
21. Ackermann, R. J.; Thorn, R. J.; Alexander, C.; Tetenbaum, M., Free Energies of Formation of Gaseous Uranium, Molybdenum, and Tungsten Trioxides. *J Phys Chem-Us* **1960,** *64* (3), 350-355.
22. Marçalo, J.; Gibson, J. K., Gas-Phase Energetics of Actinide Oxides: An Assessment of Neutral and Cationic Monoxides and Dioxides from Thorium to Curium. *J Phys Chem A* **2009,** *113* (45), 12599-12606.
23. Denning, R. G., Electronic-Structure and Bonding in Actinyl Ions. *Struct Bond* **1992,** *79*, 215-276.
24. Rauh, E. G.; Ackermann, R. J., First Ionization-Potentials of Some Refractory Oxide Vapors. *J Chem Phys* **1974,** *60* (4), 1396-1400.
25. Vasiliu, M.; Peterson, K. A.; Dixon, D. A., Calculated Ionization Potentials of MO_3 and MO_2 for M = U, Mo, W, and Nd. *J Phys Chem A* **2020,** *124* (34), 6913-6919.
26. Wheeler, V. J.; Dell, R. M.; Wait, E., Uranium Trioxide and the UO_3 Hydrates. *J Inorg Nucl Chem* **1964,** *26* (11), 1829-1845.
27. Taylor, P.; Wood, D. D.; Duclos, A. M.; Owen, D. G., Formation of Uranium Trioxide Hydrates on UO_2 Fuel in Air Steam Mixtures Near 200-Degrees-C. *J Nucl Mater* **1989,** *168* (1-2), 70-75.
28. Hausen, D. M., Characterizing and Classifying Uranium Yellow Cakes: A Background. *Jom-J Min Met Mat S* **1998,** *50* (12), 45-47.
29. Debets, P. C., Structure of Beta-UO_3. *Acta Crystallogr* **1966,** *21*, 589-593.
30. Spano, T. L.; Shields, A. E.; Barth, B. S.; Gruidl, J. D.; Niedziela, J. L.; Kapsimalis, R. J.; Miskowiec, A., Computationally Guided Investigation of the Optical Spectra of Pure Beta-UO_3. *Inorg Chem* **2020,** *59* (16), 11481-11492.
31. Weck, P. F.; Kim, E., Layered Uranium(VI) Hydroxides: Structural and Thermodynamic Properties of Dehydrated Schoepite Alpha-$UO_2(OH)_2$. *Dalton T* **2014,** *43* (45), 17191-17199.
32. Christ, C. L.; Clark, J. R., Crystal Chemical Studies of Some Uranyl Oxide Hydrates. *Am Mineral* **1960,** *45* (9-10), 1026-1061.
33. Bergstrom, G.; Lundgren, G., X-Ray Investigations on Uranyl Hydroxides .1. The Crystal Structure of Beta-$UO_2(OH)_2$. *Acta Chem Scand* **1956,** *10* (4), 673-680.
34. Dawson, J. K.; Wait, E.; Alcock, K.; Chilton, D. R., Some Aspects of the System Uranium Trioxide-Water. *J Chem Soc* **1956,** (Sep), 3531-3540.
35. Drobnič, M.; Kolar, D., Calorimetric Determination of Enthalpy of Hydration of UO_3. *J Inorg Nucl Chem* **1966,** *28* (12), 2833-2835.
36. Roof, R. B.; Cromer, D. T.; Larson, A. C., Crystal Structure of Uranyl Dihydroxide $UO_2(OH)_2$. *Acta Crystallogr* **1964,** *17* (6), 701-705.
37. Hoekstra, H. R.; Siegel, S., Uranium Trioxide-Water System. *J Inorg Nucl Chem* **1973,** *35* (3), 761-779.
38. Sweet, L. E.; Blake, T. A.; Henager, C. H.; Hu, S. Y.; Johnson, T. J.; Meier, D. E.; Peper, S. M.; Schwantes, J. M., Investigation of the Polymorphs and Hydrolysis of Uranium Trioxide. *J Radioanal Nucl Ch* **2013,** *296* (1), 105-110.
39. Wilkerson, M. P.; Hernandez, S. C.; Mullen, W. T.; Nelson, A. T.; Pugmire, A. L.; Scott, B. L.; Sooby, E. S.; Tamasi, A. L.; Wagner, G. L.; Walensky, J. R., Hydration of Alpha-UO_3 Following Storage under Controlled Conditions of Temperature and Relative Humidity. *Dalton T* **2020,** *49* (30), 10452-10462.
40. Abrefah, J.; Braid, A. D.; Wang, W.; Khalil, Y.; Olander, D. R., High-Temperature Oxidation of UO_2 in Steam-Hydrogen Mixtures. *J Nucl Mater* **1994,** *208* (1-2), 98-110.
41. Privalov, T.; Schimmelpfennig, B.; Wahlgren, U.; Grenthe, I., Structure and Thermodynamics of Uranium(VI) Complexes in the Gas Phase: A Comparison of Experimental and ab Initio Data. *J Phys Chem A* **2002,** *106* (46), 11277-11282.

42. Konings, R. J. M.; Kovács, A.; Benes, O., The Thermodynamic Properties of Gaseous $UO_2(OH)_2$. *J Nucl Mater* **2017,** *496*, 163-165.
43. Li, F. M.; Byers, M. A.; Houk, R. S., Tandem Mass Spectrometry of Metal Nitrate Negative ions Produced by Electrospray Ionization. *J Am Soc Mass Spectr* **2003,** *14* (6), 671-679.
44. Franski, R.; Sobieszczuk, K.; Gierczyk, B., Mass Spectrometric Decomposition of $[M^{n+}(NO_3^-)_{n+1}]^-$ Anions Originating from Metal Nitrates $M(NO_3)_n$. *Int J Mass Spectrom* **2014,** *369*, 98-104.
45. Lucena, A. F.; Lourenço, C.; Michelini, M. C.; Rutkowski, P. X.; Carretas, J. M.; Zorz, N.; Berthon, L.; Dias, A.; Oliveira, M. C.; Gibson, J. K., et al., Synthesis and Hydrolysis of Gas-Phase Lanthanide and Actinide Oxide Nitrate Complexes: a Correspondence to Trivalent Metal Ion Redox Potentials and Ionization Energies. *Phys Chem Chem Phys* **2015,** *17* (15), 9942-9950.
46. Kovács, A.; Dau, P. D.; Marçalo, J.; Gibson, J. K., Pentavalent Curium, Berkelium, and Californium in Nitrate Complexes: Extending Actinide Chemistry and Oxidation States. *Inorg Chem* **2018,** *57* (15), 9453-9467.
47. Monteiro, B.; Bandeira, N. A. G.; Lourenço, C.; Lucena, A. F.; Carretas, J. M.; Gibson, J. K.; Marçalo, J., Chemical Evidence of the Stability of Praseodymium(V) in Gas-Phase Oxide Nitrate Complexes. *Chem Commun* **2019,** *55* (94), 14139-14142.
48. Pasilis, S.; Somogyi, A.; Herrmann, K.; Pemberton, J. E., Ions Generated from Uranyl Nitrate Solutions by Electrospray Ionization (ESI) and Detected with Fourier Transform Ion-Cyclotron Resonance (FT-ICR) Mass Spectrometry. *J Am Soc Mass Spectr* **2006,** *17* (2), 230-240.
49. Groenewold, G. S.; Oomens, J.; de Jong, W. A.; Gresham, G. L.; McIlwain, M. E.; Van Stipdonk, M. J., Vibrational Spectroscopy of Anionic Nitrate Complexes of UO_2^{2+} and Eu^{3+} Isolated in the Gas Phase. *Phys Chem Chem Phys* **2008,** *10* (8), 1192-1202.
50. Bubas, A. R.; Perez, E.; Metzler, L. J.; Rissler, S. D.; Van Stipdonk, M. J., Collision-Induced Dissociation of $[UO_2(NO_3)_3]^-$ and $[UO_2(NO_3)_2(O_2)]^-$ and Reactions of Product Ions with H_2O and O_2. *J Mass Spectrom* **2021,** *56* (3), e4705.
51. Rios, D.; Rutkowski, P. X.; Shuh, D. K.; Bray, T. H.; Gibson, J. K.; Van Stipdonk, M. J., Electron Transfer Dissociation of Dipositive Uranyl and Plutonyl Coordination Complexes. *J Mass Spectrom* **2011,** *46* (12), 1247-1254.
52. Rios, D.; Michelini, M. C.; Lucena, A. F.; Marçalo, J.; Bray, T. H.; Gibson, J. K., Gas-Phase Uranyl, Neptunyl, and Plutonyl: Hydration and Oxidation Studied by Experiment and Theory. *Inorg Chem* **2012,** *51* (12), 6603-6614.
53. Martens, J.; Berden, G.; Gebhardt, C. R.; Oomens, J., Infrared Ion Spectroscopy in a Modified Quadrupole Ion Trap Mass Spectrometer at the FELIX Free Electron Laser Laboratory. *Rev Sci Instrum* **2016,** *87* (10), 103108.
54. Kempkes, L. J. M.; Martens, J. K.; Grzetic, J.; Berden, G.; Oomens, J., Deamidation Reactions of Protonated Asparagine and Glutamine Investigated by Ion Spectroscopy. *Rapid Commun Mass Sp* **2016,** *30* (4), 483-490.
55. Berden, G.; Derksen, M.; Houthuijs, K. J.; Martens, J.; Oomens, J., An automatic variable laser attenuator for IRMPD spectroscopy and analysis of power-dependence in fragmentation spectra. *Int J Mass Spectrom* **2019,** *443*, 1-8.
56. Devlin, F. J.; Stephens, P. J., Ab-Initio Calculation of Vibrational Circular-Dichroism Spectra of Chiral Natural-Products Using Mp2 Force-Fields - Camphor. *J Am Chem Soc* **1994,** *116* (11), 5003-5004.
57. Cao, X. Y.; Dolg, M.; Stoll, H., Valence Basis Sets for Relativistic Energy-Consistent Small-Core Actinide Pseudopotentials. *J Chem Phys* **2003,** *118* (2), 487-496.
58. Cao, X. Y.; Dolg, M., Segmented Contraction Scheme for Small-Core Actinide Pseudopotential Basis Sets. *J Mol Struc-Theochem* **2004,** *673* (1-3), 203-209.

59. Weigend, F.; Ahlrichs, R., Balanced Basis Sets of Split Valence, Triple Zeta Valence and Quadruple Zeta Valence Quality for H to Rn: Design and Assessment of Accuracy. *Phys Chem Chem Phys* **2005,** *7* (18), 3297-3305.

60. Rappoport, D.; Furche, F., Property-Optimized Gaussian Basis Sets for Molecular Response Calculations. *J Chem Phys* **2010,** *133* (13), 134105.

61. Frisch, M. J.; Trucks, G. W.; Schlegel, H. B.; Scuseria, G. E.; Robb, M. A.; Cheeseman, J. R.; Scalmani, G.; Barone, V.; Mennucci, B.; Petersson, G. A., et al. *Gaussian 09, Revision D.01*, Gaussion, Inc.: Wallingford, CT, 2009.

62. de Jong, W. A.; Apra, E.; Windus, T. L.; Nichols, J. A.; Harrison, R. J.; Gutowski, K. E.; Dixon, D. A., Complexation of the Carbonate, Nitrate, and Acetate Anions with the Uranyl Dication: Density Functional Studies with Relativistic Effective Core Potentials. *J Phys Chem A* **2005,** *109* (50), 11568-11577.

63. Forney, D.; Thompson, W. E.; Jacox, M. E., The Vibrational-Spectra of Molecular-Ions Isolated in Solid Neon. XI. NO_2^+, NO_2^-, and NO_3^-. *J Chem Phys* **1993,** *99* (10), 7393-7403.

64. Smith, D.; James, D. W.; Devlin, J. P., Vibrational Spectra Molecular Metal Nitrate Monomers and Dimers. *J Chem Phys* **1971,** *54* (10), 4437-4442.

65. Vaska, L., Dioxygen-Metal Complexes - Toward a Unified View. *Accounts Chem Res* **1976,** *9* (5), 175-183.

66. Groenewold, G. S.; Van Stipdonk, M. J.; de Jong, W. A.; Oomens, J.; Gresham, G. L.; McIlwain, M. E.; Gao, D.; Siboulet, B.; Visscher, L.; Kullman, M., et al., Infrared Spectroscopy of Dioxouranium(V) Complexes with Solvent Molecules: Effect of Reduction. *Chemphyschem* **2008,** *9* (9), 1278-1285.

67. Vallet, V.; Wahlgren, U.; Grenthe, I., Probing the Nature of Chemical Bonding in Uranyl(VI) Complexes with Quantum Chemical Methods. *J Phys Chem A* **2012,** *116* (50), 12373-12380.

68. Nguyen-Trung, C.; Begun, G. M.; Palmer, D. A., Aqueous Uranium Complexes .2. Raman-Spectroscopic Study of the Complex-Formation of the Dioxouranium(VI) Ion with a Variety of Inorganic and Organic-Ligands. *Inorg Chem* **1992,** *31* (25), 5280-5287.

69. Gronert, S., Estimation of Effective Ion Temperatures in a Quadrupole Ion Trap. *J Am Soc Mass Spectr* **1998,** *9* (8), 845-848.

70. Gong, Y.; Vallet, V.; Michelini, M. D.; Rios, D.; Gibson, J. K., Activation of Gas-Phase Uranyl: From an Oxo to a Nitrido Complex. *J Phys Chem A* **2014,** *118* (1), 325-330.

71. Johnson, T. J.; Sweet, L. E.; Meier, D. E.; Mausolf, E. J.; Kim, E.; Weck, P. F.; Buck, E. C.; McNamara, B. K., Time-Resolved Infrared Reflectance Studies of the Dehydration-Induced Transformation of Uranyl Nitrate Hexahydrate to the Trihydrate Form. *J Phys Chem A* **2015,** *119* (39), 9996-10006.

72. Fortier, S.; Hayton, T. W., Oxo Ligand Functionalization in the Uranyl Ion (UO_2^{2+}). *Coordin Chem Rev* **2010,** *254* (3-4), 197-214.

73. Rios, D.; Michelini, M. D.; Lucena, A. F.; Marçalo, J.; Gibson, J. K., On the Origins of Faster Oxo Exchange for Uranyl(V) versus Plutonyl(V). *J Am Chem Soc* **2012,** *134* (37), 15488-15496.

74. Dau, P. D.; Maurice, R.; Renault, E.; Gibson, J. K., Heptavalent Neptunium in a Gas-Phase Complex: $(Np^{VII}O_3^+)(NO_3^-)_2$. *Inorg Chem* **2016,** *55* (19), 9830-9837.

75. Michelini, M. D.; Marcalo, J.; Russo, N.; Gibson, J. K., Gas-Phase Reactions of Uranate Ions, UO_2^- , UO_3-, UO_4^-, and UO_4H^-, with Methanol: a Convergence of Experiment and Theory. *Inorg Chem* **2010,** *49* (8), 3836-3850.

76. Ronchi, C.; Capone, F.; Colle, J. Y.; Hiernaut, J. P., Volatile molecule PuO3 observed from subliming plutonium dioxide. *J Nucl Mater* **2000,** *280* (1), 111-115.

77. Kovács, A., Relativistic Multireference Quantum Chemical Study of the Electronic Structure of Actinide Trioxide Molecules. *J Phys Chem A* **2017,** *121* (12), 2523-2530.

78. Zaitsevskii, A., Plutonium and Transplutonium Element Trioxides: Molecular Structures, Chemical Bonding, and Isomers. *Phys Chem Chem Phys* **2015,** *17* (38), 24831-24836.

TOC Graphic